Acta Materialia 99 (2015) 206–212

Contents lists available at ScienceDirect

Acta Materialia

journal homepage: www.elsevier.com/locate/actamat

Spiral fracture in metallic glasses and its correlation with failure criterion

Xianqi Lei [a], Yujie Wei [a,*], Bingchen Wei [a], Wei-Hua Wang [b]

[a] LNM, Institute of Mechanics, Chinese Academy of Sciences, Beijing 100190, PR China
[b] Institute of Physics, Chinese Academy of Sciences, Beijing 100080, PR China

ARTICLE INFO

Article history:
Received 24 May 2015
Revised 3 August 2015
Accepted 3 August 2015

Keywords:
Metallic glasses
Failure criterion
Mohr–Coulomb
Spiral fracture

ABSTRACT

We report the observation of spiral fracture of the metallic glass $Zr_{41}Ti_{14}Cu_{12.5}Ni_{10}Be_{22.5}$ (at.%) subjected to both shear and normal stresses. The spiral angle (that between the spiral line and the loading axis) increases as we gradually change the normal stress from tensile (positive) to compressive (negative). The spiral nature of the fractured surface leads to a left-handed helix fractography pattern in tension, and a right-handed helix in compression. The Mohr–Coulomb type of failure is essential for the unique spiral fracture. The use of spiral angles resulted from torsion–tension experiments provide another novel experimental strategy to examine the failure criterion as well as stress state dependence of deformation mechanisms which lead to failure in metallic glasses.

1. Introduction

The pressure sensitivity of failure in metallic glasses has been a topic of active research since the early experimental work of Davis and Kavesh [1] on ribbons, and more recent work by a number of authors [1–7]. This topic is tied to understanding the fundamental aspects of plastic deformation mechanisms which are still not fully understood [2,8]. Experimentally, the pressure sensitivity of failure can be directly examined by conducting experiments with superimposed hydrostatic pressure [1,3–7] in the manner of Bridgman [9], while any tension/compression asymmetry that exists at one atmosphere may also indicate some pressure sensitivity. For example, tension and compression tests conducted at one atmosphere by Donovan [10] found that the failure strength of $Pd_{40}Ni_{40}P_{20}$ followed the Mohr–Coulomb failure (M–C) criterion. Various works by Lewandowski et al. [3–7] found only a moderate normal stress or pressure sensitivity for tests conducted with superimposed hydrostatic pressure when analyzed with either a M–C or Drucker–Prager (D–P) criterion, despite relatively large changes in fracture angle [3–5] going from tension to compression at atmospheric pressure. This asymmetry in fracture angle was later shown to be influenced by stress concentrations at the sample/platen interface that biased the compression fracture angles, later rectified by the design of tapered grips [11,12]. Other recent work by Lu and Ravichandran [13] utilized confined compression tests on $Zr_{41.2}Ti_{13.8}Cu_{12.5}Ni_{10}Be_{22.5}$ and found a more significant effect of confinement, although frictional restraint of the confining rings may have affected the magnitude of the pressure effect reported. Earlier work [14] utilized tension, compression, and torsion samples on a similar material and suggested that a von Mises criterion (i.e. pressure independent) might be appropriate. All of these previous works highlight the importance of continuing to examine the effects of changes in stress state and loading mode, as these have been observed to affect the deformation and fracture toughness, as shown by others [15–17].

In addition to experimental characterization, computational techniques were also employed to examine the validity of broadly used strength criteria including the Mohr–Coulomb criteria, Drucker–Prager criterion (D–P), and von Mises criterion. By using atomistic simulations, Lund and Schuh in 2004 [18] found that a pressure or normal stress dependence must be included in the failure criterion of metallic glasses, and they also suggested a range of Mohr–Coulomb internal friction coefficient of $\alpha = 0.12–0.4$ [19,20]. These atomistic simulations often produced much higher values for the friction coefficient than what was obtained experimentally, as well as what is found presently. Instrumented indentation and finite element simulations have also been employed to examine the pressure sensitivity of strength in BMGs [21–24] and they all suggested that pressure sensitive M–C or D–P [25] were better suited to capture deformation in structures with complex stress state. Finite-element modeling with embedded M–C criterion is able to captured typical features seen from systematic experimental characterizations of BMGs [26]. Later on simulations by Zhao and Li

---

* Corresponding author.
E-mail address: yujie_wei@lnm.imech.ac.cn (Y. Wei).

http://dx.doi.org/10.1016/j.actamat.2015.08.008
1359-6454/

[27] showed that taking consideration free volume dilatation [28] and the pressures sensitive D–P failure criterion are sufficient to explain the tension–compression fracture asymmetry in BMGs. Note that aforementioned experiments were typically performed at room temperature or temperature far below their respective glass transition temperatures of the tested materials. Recent work by Thamburaja et al. [29], guided by a series of molecular dynamics simulations conducted at low-homologous temperatures under homogeneous deformations, quantitatively prove that the continuum plastic behavior in metallic glasses could be described by the von Mises-type plastic yield criterion in that particular.

It is now generally accepted that criteria taking pressure sensitivity into account such as the M–C and the D–P are more appropriate to describe the strength of BMGs than pressure-independent ones like the Mises criterion when BMGs were tested at a temperature far below their glass transition temperature. However, regarding the exact formula to quantify the contribution of pressure to failure in BMGs, it remains an open question. For example, Zhang et al. suggested a modified M–C criterion where the internal friction parameters are different in tension and compression surface stress states [30]. Chen et al. [31] proposed an eccentric elliptical criterion on the basis of atomistic potential analysis. Later on, Wei [32,33] considered the different contributions of the distortional part and the volumetric part in total strain energy density to failure, and developed an energy based criterion where the shear strength and the normal strength are considered as two independent material parameters in BMGs. Recent experiments by Lei et al. [34] indeed found that distinct shear strength and normal strength are responsible for notch strengthening in BMGs: The tensile strength of the net section in circumferentially notched cylindrical BMGs increases with the constraint quantified by the ratio of notch depth over notch root radius. In summary, substantial understanding has been developed about the strength criterion of BMGs in the last two decades. Quantitatively, existing data about the material parameters of BMGs in different failure criteria are very scattered. There are compelling needs to critically examine the applicability of different failure criteria and to explore novel experimental strategies for calibration. In this work, we conducted combined torsion–tension experiments on $Zr_{41}Ti_{14}Cu_{12.5}Ni_{10}Be_{22.5}$ bulk metallic glass rods, and we further validated the applicability of Mohr–Coulomb failure criterion on the tested metallic glasses from the spiral fracture angle aspect. In contrast to the classic torsion–tension tests to a polycrystalline thin-walled tube by Taylor and Quinney in 1931 [35], the metallic glass could be better suited for failure analysis because the onset of plastic flow in polycrystalline materials is very likely to be influenced by preferred orientations of individual grains [36].

2. Experimental

We use probably the most well investigated BMG $Zr_{41}Ti_{14}Cu_{12.5}Ni_{10}Be_{22.5}$ (at.%). It represents a substantial amount of existing BMGs which offer almost no tensile ductility but exhibit intermediate-to-high resistance to fracture. The material is made in a water-cooled arc-melting hearth under a titanium-gathered argon atmosphere. Elemental metals (>99.9% purity) are used to form the master alloy and suction-casted into a $\varnothing 8 \times 100$ mm cylinders. Those cylinders are then lathed using carbide tool into dog-bone samples with dimensions shown as Fig. 1a and b. The gauged sections of the samples are then mirror-polished to smooth the surface. A servo-hydraulic MTS 809 test system is used to do the torsion–tension tests. We first exerted prescribed axial normal load within 20 s. This loading condition corresponds to a strain rate on the order of 10^{-3}/s since $Zr_{41}Ti_{14}Cu_{12.5}Ni_{10}Be_{22.5}$ breaks after an elastic strain limit about 0.02. We then twist the samples to failure. The torsion is applied at an angular velocity of 5°/min (corresponding to a maximum shear strain rate of about 2.5×10^{-4}/s). We also conducted contrast experiments with torsion loaded first (4 Nm/min, corresponding to a maximum shear strain rate about 1.2×10^{-5}/s), then axial load next (0.2 mm/min, corresponding to a strain rate about 2.5×10^{-4}/s), to character the normal–shear failure stresses combination's dependence on loading path. The range of the axial normal stress σ_0 (see Fig. 1c) for the tested samples is from $\sigma_0 = 1.98$ GPa (uniaxial tension) to $\sigma_0 = -1.84$ GPa, and is listed in detail in Table 1.

3. Results and discussion

As a BMG sample (see layout and dimensions in Fig. 1a and b) is subjected to mechanical twist while an exact axial load is applied, any material point in the sample is subjected to two stress components: the axial normal stress σ_0 and the shear stress (as illustrated in Fig. 1c). The shear deformation along the radial direction in a crossection perpendicular to the cylinder axis is linear in nature (as seen in Fig. 1d), resulting in a linear variation in shear stress

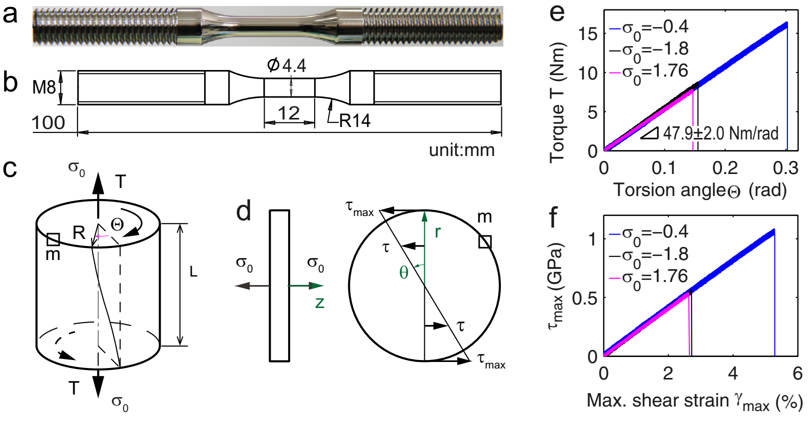

Fig. 1. Mechanical characterization of cylindrical metallic glass Zr_{41} $Ti_{14}Cu_{12.5}Ni_{10}Be_{22.5}$ subjected to both normal and shear stress. (a) Sample layout. (b) Dimensions of sample for normal loading-torsion tests (unit: mm). (c) Illustration of the loading: σ_0 – axial normal loading; T – torque; Θ – twisting angle; R – sample radius; L – length of interest; m – an arbitrary material point at the outermost surface. (d) Projected view to show normal stress σ_0 along the sample axis and radical shear stress τ distribution in the cross-section perpendicular to the normal direction; τ_{max} – the maximum shear stress at the outermost surface. (e) Typical torque versus twist angle curves at different axial normal stress; and we reach a stiffness of 47.9 ± 2.0 Nm/rad based on all experiments data listed in Table 1. (f) The maximum shear stress $\tau_{max}(\tau_{max} = 2T/\pi R^3)$ versus the maximum shear strain $\gamma_{max}(\gamma_{max} = \Theta R/L)$ at a material point in outermost surface.

Table 1
Detailed experiment data about tension torsion of $Zr_{41}Ti_{14}Cu_{12.5}Ni_{10}Be_{22.5}$ samples. The axial normal stress σ_0 and the maximum shear stress τ_{max} at failure, the torsion torque T at failure, the torsion twist angle Θ at failure, the spiral fracture angle $\theta + \beta$, and sample size R-radius are shown. Data in rows with "*" come from contrast experiments in which we apply torsion first, keep it constant at a target value, and then gradually increase the magnitude of normal axial stress till the sample fails.

No.	σ_0 (GPa)	τ_{max} (GPa)	T (Nm)	Θ (rad)	$\theta + \beta$ (°)	$2R$ (mm)	No.	σ_0 (GPa)	τ_{max} (GPa)	T (Nm)	Θ (rad)	$\theta + \beta$ (°)	$2R$ (mm)
1	1.886	0.000	0.00	0.000	54.4	4.00	27	0.000	0.992	14.85	0.299	90.0	4.24
2	1.950	0.000	0.00	0.000	56.1	4.22	28	−0.166	1.012	14.72	0.274	93.5	4.20
3	1.980	0.000	0.00	0.000	58.0	4.29	29	−0.170	0.961	10.94	0.276	99.9	3.87
4*	1.977	0.120	1.67	0.033	50.0	4.16	30	−0.200	1.071	15.44	0.317	97.7	4.19
5*	1.884	0.334	4.85	0.100	70.0	4.20	31	−0.360	0.994	14.46	0.284	102.6	4.20
6*	1.852	0.353	5.07	0.100	68.5	4.18	32	−0.420	1.061	16.08	0.302	103.7	4.26
7	1.756	0.490	7.65	0.147	67.0	4.30	33	−0.420	1.048	15.81	0.304	106.4	4.25
8	1.668	0.467	7.23	0.142	67.0	4.28	34	−0.426	0.996	14.71	0.267	103.0	4.22
9	1.571	0.547	8.38	0.162	73.0	4.27	35	−0.480	1.001	15.64	0.278	102.7	4.30
10	1.530	0.565	8.11	0.170	69.0	4.18	36	−0.500	1.029	15.49	0.294	103.6	4.25
11	1.362	0.660	10.10	0.204	73.0	4.27	37	−0.560	1.030	15.52	0.296	102.8	4.25
12	1.281	0.772	11.48	0.252	78.7	4.23	38	−0.580	1.000	14.42	0.263	105.4	4.19
13	1.168	0.765	11.43	0.234	78.0	4.24	39	−0.729	0.926	13.22	0.239	109.0	4.18
14*	1.078	0.819	12.01	0.229	80.0	4.21	40	−0.740	0.877	8.80	0.278	103.6	3.73
15	1.070	0.854	12.61	0.270	77.7	4.22	41	−0.866	0.958	13.92	0.260	107.0	4.20
16	1.040	0.821	12.64	0.267	72.6	4.28	42	−1.006	0.879	12.88	0.239	110.5	4.21
17	0.956	0.837	12.55	0.264	75.8	4.24	43	−1.124	0.904	13.10	0.232	107.0	4.19
18	0.860	0.913	13.76	0.288	84.6	4.25	44	−1.245	0.878	12.48	0.224	107.1	4.17
19	0.733	0.888	13.57	0.273	87.1	4.27	45	−1.342	0.838	12.07	0.222	118.6	4.19
20	0.630	1.008	15.52	0.352	88.8	4.28	46	−1.485	0.769	10.70	0.191	121.0	4.14
21	0.531	0.931	13.91	0.279	82.6	4.24	47*	−1.605	0.814	12.09	0.222	120.0	4.23
22	0.400	0.998	16.39	0.343	83.0	4.37	48	−1.660	0.770	11.48	0.204	120.8	4.24
23	0.323	0.955	13.99	0.278	90.4	4.21	49*	−1.784	0.593	8.75	0.161	124.5	4.22
24*	0.287	1.006	15.05	0.285	80.0	4.24	50	−1.838	0.620	8.48	0.155	123.4	4.12
25	0.200	1.040	16.48	0.328	88.3	4.32	51*	−1.848	0.456	6.64	0.134	125.5	4.20
26	0.000	1.068	14.18	0.284	95.2	4.07							

along the radius. We show in Fig. 1e three typical torque-twisting angle curves for an arbitrary material point in the outer-most surface of the sample under different axial normal stress $\sigma_0 = -1.8$ GPa (black), $\sigma_0 = -0.4$ GPa (blue) and $\sigma_0 = 1.76$ GPa (purple), and we reach a stiffness of 47.9 ± 2.0 Nm/rad basing on all the test samples (see listed in detail in Table 1); and we show in Fig. 1f the three typical maximum shear stress versus its respect maximum shear strain curves with respect to Fig. 1e. The failure points supply information about the critical combination of shear stress and normal stress which lead to failure.

A set of tension–torsion data are obtained as we gradually change the pre-applied normal stress from tension to compression. We show in Fig. 2 the critical combinations of maximum shear stress τ_{max} and axial normal stress σ_0 which lead to failure in the principal stress coordinate. Theoretical predictions by the M–C criterion, the Mises criterion, and the D–P criterion, by using the least square fittings, are also shown. For the metallic glass $Zr_{41}Ti_{14}Cu_{12.5}Ni_{10}Be_{22.5}$ tested here, the yielding point, where the strength maximizes, is also where fracture occurs. There is no perceivably macroscopic yielding before failure, as seen in the torque–twist angle curves in Fig. 1e. We hence use the term "failure" instead of "yielding" to describe the critical combinations of shear and normal stress which trigger fracture in $Zr_{41}Ti_{14}Cu_{12.5}Ni_{10}Be_{22.5}$. It is noted that there could be possibilities when shear banding does not lead to catastrophic failure, for example in bending tests [37] and in indentation experiments [21–24]. In those states of stress, "yielding" apparently differs from "failure". In the M–C criterion,

$$|\tau_n| = c - \sigma_n \tan\phi \tag{1}$$

where material parameters c and ϕ are respectively the cohesion of a material and the angle of the internal friction. For a given stress state leading to failure, τ_n is the shear strength along the failure surface, and σ_n is the normal stress at the failure surface. By convention, we let $\sigma_n > 0$ correspond to a tensile stress and $\sigma_n < 0$ a compressive stress. We may express τ_n and σ_n in terms of the principal stresses σ_1, σ_2 and σ_3 (with $\sigma_1 \geqslant \sigma_2 \geqslant \sigma_3$ and $\sigma_2 = 0$ in this work):

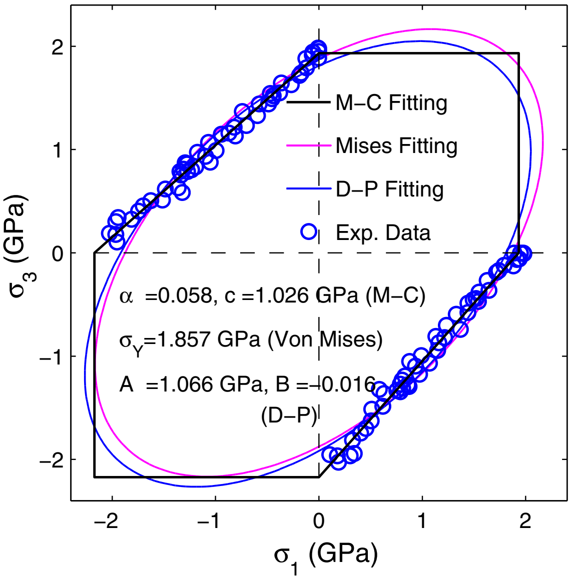

Fig. 2. The failure envelope of metallic glass Zr_{41} $Ti_{14}Cu_{12.5}Ni_{10}Be_{22.5}$ subjected to both normal and shear stress. We plot the experimental data against predictions by Mohr–Coulomb (M–C), Mises and Druck–Prager (D–P) failure criterion. An internal friction coefficient of $\alpha = 0.058 \pm 0.012$ and a cohesion $c = 1.026 \pm 0.014$ GPa are used for the M–C criterion; the equivalent strength of $\sigma_Y = 1.857 \pm 0.117$ GPa is used in the Mises criterion; and an internal friction coefficient of $A = 1.066 \pm 0.018$ GPa and $B = -0.016 \pm 0.008$ are used in the D–P criterion. The D–P and M–C values are consistent with Lewandowiski's report [3] using superimposed method.

$$\tau_n = \frac{\sigma_1 - \sigma_3}{2}\cos\phi, \quad \text{and } \sigma_n = \frac{\sigma_1 + \sigma_3}{2} + \frac{\sigma_1 - \sigma_3}{2}\sin\phi \tag{2}$$

In that manner, Eq. (1) can be reformulated as:

$$\sigma_1 - \sigma_3 = 2c\cos\phi - (\sigma_1 + \sigma_3)\sin\phi \tag{3}$$

From Eq. (3), it is convenient to obtain c and ϕ for any two independent critical combinations of shear stress and normal stress.

Normally, c and ϕ are derived by employing data from uniaxial tension ($\sigma_1 = \sigma_s^t, \sigma_3 = 0$) and compression ($\sigma_1 = 0, \sigma_3 = -\sigma_s^c$) tests, where σ_s^t and σ_s^c are respectively the tensile strength and the compressive strength. In that case, one may write the internal friction coefficient α and the cohesion c as

$$\alpha = \tan\phi = \tan\left[\sin^{-1}\left(\frac{\sigma_s^c - \sigma_s^t}{\sigma_s^c + \sigma_s^t}\right)\right], \quad 2c = \sqrt{\sigma_s^c \sigma_s^t} \tag{4}$$

Given the fluctuation of measured strengths [38,39], the internal friction coefficient α determined by Eq. (4) may vary significantly, which could be evidently seen from the scattering of α from literature. Part of this variation in α obtained from compression tests could arise from stress concentrations that occur in compression that bias the fracture angle, as well as defects in the material [11,12]. To circumvent the sensitivity of α to strength fluctuation, we use the least square fitting to obtain c and ϕ. As shown in Fig. 2, the least square fitting to Eq. (3) yields $\alpha = 0.058 \pm 0.012$ and $c = 1.026 \pm 0.014$ GPa.

In the same manner, the strength σ_Y in the Mises criterion is obtained by the least square fitting of the equation

$$\sqrt{\frac{1}{2}\left[(\sigma_1 - \sigma_2)^2 + (\sigma_1 - \sigma_3)^2 + (\sigma_2 - \sigma_3)^2\right]} = \sigma_Y \tag{5}$$

to experimental data in Fig. 2, with $\sigma_2 = 0$ in this work. The least square fitting leads to $\sigma_Y = 1.857 \pm 0.117$ GPa. The conventional D–P [25] criterion can be expressed in terms of principal stresses σ_1, σ_2 and σ_3 (with $\sigma_1 \geqslant \sigma_2 \geqslant \sigma_3$ and $\sigma_2 = 0$ in this work) as well:

$$\sqrt{\frac{1}{6}\left[(\sigma_1 - \sigma_2)^2 + (\sigma_1 - \sigma_3)^2 + (\sigma_2 - \sigma_3)^2\right]} = A + B(\sigma_1 + \sigma_2 + \sigma_3) \tag{6}$$

The parameter A reflects the role of the equivalent stress (or von Mises stress) while B is a dimensionless coefficient which quantifies the contribution of the hydrostatic (or mean) stress. In the absence of pressure sensitivity, A is exactly the shear strength used in the von Mises criterion. Both parameters could be determined from experiments. As D–P criterion was also applied to the deformation of metallic glasses to capture its pressure dependent failure and plastic flow behavior [22–24]. We present the predictions by the D–P criterion with $A = 1.066 \pm 0.018$ GPa and $B = -0.016 \pm 0.008$ from the least square fitting using Eq. (6). As seen in Fig. 2, the curve from D–P criterion prediction is close to that by the M–C criterion in most regime of the normal stress, which explains why both criteria can capture the deformation of metallic glasses in certain boundary-value problems [21–24]. The D–P and M–C values are very consistent with Lewandowiski's report [3] using superimposed method. We further note that parameters A and B in Eq. (6) obtained by least square fitting to the experimental data may be deduced from the two material constants in the M–C criterion in Eq. (3):

$$A = \frac{6c\cos\phi}{\sqrt{3}(3 - \sin\phi)}, \quad B = \frac{2\sin\phi}{\sqrt{3}(3 - \sin\phi)} \tag{7}$$

The two sets of parameters obtained from different strategies, however, may be not necessarily to be the same. Usually, the least square fitting method can supply better accuracy.

The fitted tension and compression strength from the Mohr–Coulomb criterion agree well with literature reports [3,14], especially with Bruck et al.'s [14] reports of uniaxial tensile strength $\sigma_s^t = 1.93 \pm 0.03$ GPa, and a uniaxial compression strength of $\sigma_s^c = 2.12 \pm 0.05$ GPa with the same kind of BMGs. However, they [14] suggested that BMGs follow the pressure independent Mises criterion. In our results shown in Fig. 2, while a Mises strength of $\sigma_Y = 1.857 \pm 0.117$ GPa in Eq. (5) can fit most of the region, there is apparent deviation of the theory from experimental data, in particular as the normal stress approaches the compressive strength. The friction coefficient $\alpha = 0.058 \pm 0.012$ and cohesion $c = 1.026 \pm 0.014$ GPa from M–C fitting agree well with literature reports for samples tested with superimposed hydrostatic pressure by Davis et al. [1] and Lewandowski et al. [3–7]. This confirms that the failure strength in Vitreloy 1 is only moderately normal stress/pressure-dependent when failure occurs by shear. However, inclusion-initiated failure has been shown to change this dependence [17].

It is of interest to examine whether the loading path would influence the critical combinations of normal–shear stresses shown in Fig. 2. We demonstrate this effect by conducting two contrast groups of experiments. We first report the shear stress versus loading time in Fig. 3a, note here a constant tensile normal stress $\sigma_0 = 1.070$ GPa is exerted. The sample failures at a critical shear stress $\tau_{max} = 0.854$ GPa. In the second experiment (see Fig. 3b), we first apply torsion to the sample and then maintain the applied torsion when the maximum shear stress satisfies $\tau_{max} = 0.819$ GPa – a value very close to the critical shear stress in Fig. 3a, then the sample is subjected to tension till its failure at an axial normal stress $\sigma_0 = 1.078$ GPa. Similar contrast experiments were performed when the normal stress is compressive. In Fig. 3c, we presented torsion induced failure when a constant compressive normal stress $\sigma_0 = -1.660$ GPa is first applied, corresponding critical shear stress is $\tau_{max} = 0.770$ GPa. Alternatively, when we maintain the shear stress to be constant $\tau_{max} = 0.814$ GPa, the critical normal compressive stress is $\sigma_0 = -1.605$ GPa. While there are small difference between the combination of normal–shear stress due to the load-control difficulty in experiments, our contrast experiments shown in Fig. 3 suggest that the critical combination of stresses shown in Fig. 2 is independent on loading path.

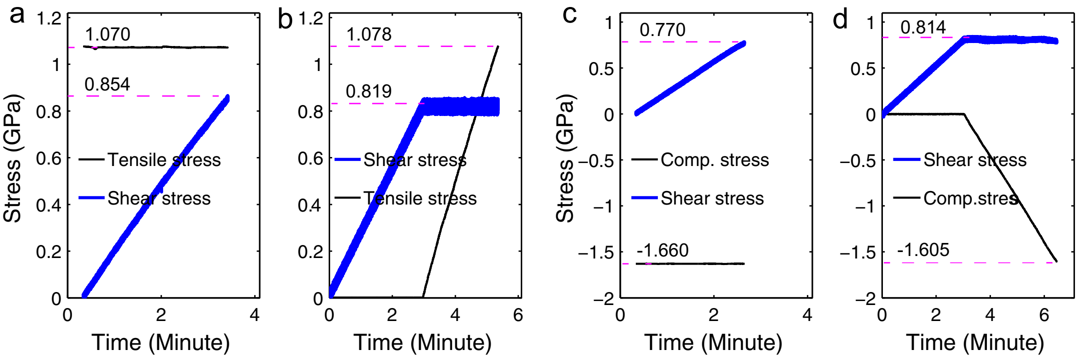

Fig. 3. Independence of loading paths for the critical combination of shear–normal stress. (a) Torsion failure under a tensile normal stress state ($\sigma_0 = 1.070$ GPa, $\tau_{max} = 0.854$ GPa). (b) Tensile failure under a shear stress state ($\sigma_0 = 1.078$ GPa, $\tau_{max} = 0.819$ GPa). (c) Torsion failure under a compressive normal stress state ($\sigma_0 = -1.660$ GPa, $\tau_{max} = 0.770$ GPa). (d) Compress to failure under a shear stress state ($\sigma_0 = -1.605$ GPa, $\tau_{max} = 0.814$ GPa).

We further check the fractographies of the failed samples under mixing loading. Typically, the fractured samples subjected to tension and concurrent torsion show spiral fracture, as evidently seen in the scanning electron microscope images shown in Fig. 4. For completeness, we also show the fractographies of the metallic glass Zr_{41} $Ti_{14}Cu_{12.5}Ni_{10}Be_{22.5}$ under simple tension (Fig. 4a) and simple compression (Fig. 4i). The fractured angle in tension is about 58°, and that in compression is about $180° - 136.8° = 43.2°$, in excellent agreement with previous report [40]. In Fig. 4b–h, we show failed samples at different critical shear–normal stress combinations while the normal stress decreases from $\sigma_0 = 1.28$ GPa to $\sigma_0 = -0.58$ GPa, respectively. It is interesting to see when a sample fails under shear (induced by clockwise torsion) and compressive normal stress, the fractured surface and the cylindrical surface form a right-hand spiral (Fig. 4f–h). In contrast, a left-hand spiral forms as the normal stress is tensile (Fig. 4b–d). In Fig. 4j, we show how we define a characteristic spiral angle $\theta + \beta$, which is the angle between the fracture surface and the axial stress direction. Here θ is the angle between the fracture surface and the max principal stress σ_1 and β is the angle between the axial stress σ_0 and σ_1 directions, as demonstrated in Fig. 4k.

Under classical Mohr–Coloumb strength criterion, the angle θ is constant, as illustrated in Fig. 5a. In this work, the equivalent internal friction angle $\phi = 3.3°$, which leads to $\theta = 46.65°$. As β is the angle between the normal stress σ_0 and the max principal stress σ_1, as demonstrated in Fig. 4k, we may write β in terms of α and c in the Mohr–Coulomb strength criterion:

$$\beta = \tan^{-1}\left(\frac{\tau_{max}}{\sigma_1}\right) \quad \text{with} \begin{cases} \sigma_1 = \frac{2c\cos\phi + \sigma_0(1-\sin\phi)}{2} \\ \tau_{max} = \frac{\sqrt{(2c\cos\phi - \sigma_0\sin\phi)^2 - \sigma_0^2}}{2} \end{cases} \tag{8}$$

We may now apply Eq. (8), with $\alpha = 0.058$ and $c = 1.026$ GPa from Fig. 2 to calibrate the applicability of the M–C strength criterion. We show in Fig. 5b the measured spiral fracture angle $\theta + \beta$ (symbols) as a function of the normal stress σ_0. The solid purple line is the theoretical predictions by using Eq. (8), and it can be seen that the difference between the predictions from Eq. (8) and those from experiments is marginally small. When a sample is subjected to simple tension and the normal stress σ_0 being the maximum principal stress σ_1, we $\beta = 0$ and $\theta = \pm(\frac{\pi}{4} + \frac{\phi}{2})$.

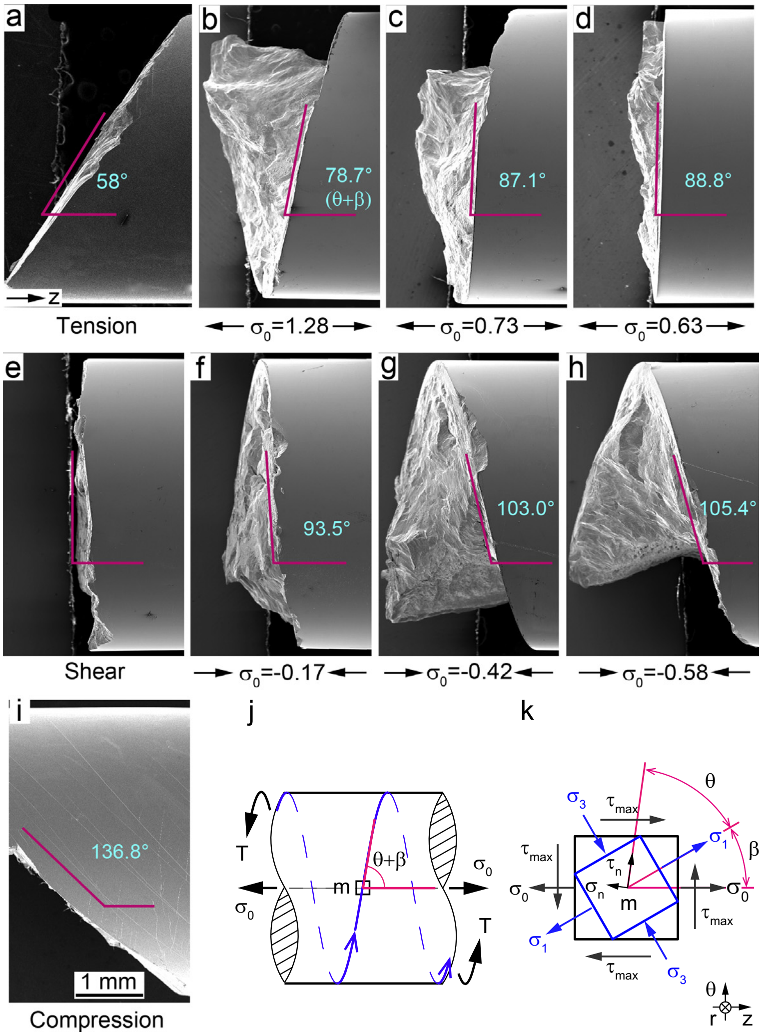

Fig. 4. Spiral fracture of the metallic glass $Zr_{41}Ti_{14}Cu_{12.5}Ni_{10}Be_{22.5}$ subjected to shear and normal stresses. (a) Fracture angle under uniaxial tension. (b)–(h) Variation of spiral fracture angles at different critical maximum shear stress τ_{max} and axial normal stress σ_0: (b) $\sigma_0 = 1.28$, $\tau_{max} = 0.77$; (c) $\sigma_0 = 0.73$, $\tau_{max} = 0.89$; (d) $\sigma_0 = 0.63$, $\tau_{max} = 1.00$; (e) $\sigma_0 = 0$, $\tau_{max} = 0.99$; (f) $\sigma_0 = -0.17$, $\tau_{max} = 0.96$; (g) $\sigma_0 = -0.42$, $\tau_{max} = 1.05$; (h) $\sigma_0 = -0.58$, $\tau_{max} = 1.00$ (unit, GPa). (i) Fracture angle under uniaxial compression, and the angle value agree well with Jiang et al.'s report [40]. (j) Illustration to show the definition of angle $\theta + \beta$ to characterize the spiral fracture. (k) Stress components in different coordinates and the relationship between the angles and the stress: θ is the angle between the spiral fracture edge and the maximum principal stress σ_1, and β is the angle between the normal stress σ_0 and the maximum principal stress σ_1; σ_n is normal stress, e.g. the normal stress at the fracture surface, and τ_n is the relative shear stress.

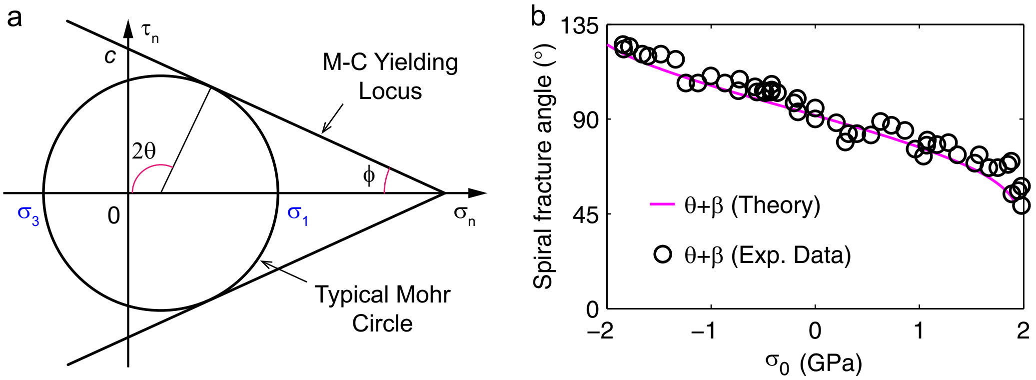

Fig. 5. Spiral fracture angle as a function of normal stress state: comparison between experimental data and theoretical prediction. (a) Illustration of the critical angles in the Mohr–Coulomb strength criterion. (b) Dependence of the spiral fracture angle $\theta + \beta$ on the applied normal stress: theoretical predictions against experimental measurement (Solid red: prediction by Eq. (8)). (For interpretation of the references to color in this figure legend, the reader is referred to the web version of this article.)

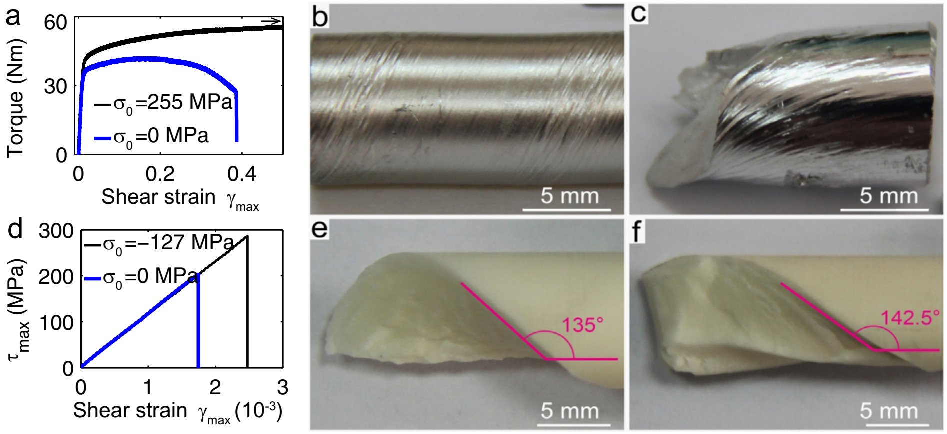

Fig. 6. Mechanical response of ductile Al 6061 and brittle ceramic Al_2O_3 under torsion–tension loading. (a) The torque-shear strain curve of Al 6061 subjected to two different tensile normal stress $\sigma_0 = 0$ (blue) and 255 MPa (black). (b) The surface pattern of sample with $\sigma_0 = 0$ MPa and an outermost shear strain of 200%. (c) Necking to shear failure in Al 6061 when $\sigma_0 = 255$ MPa, which is consistent with typical failure mode in materials governed by Mises type of plastic flow. (d) The maximum shear stress and the maximum shear strain curve of ceramic Al_2O_3 with stress $\sigma_0 = 0$ MPa (blue) and $\sigma_0 = -127$ MPa (black). (e) and (f) Failure pattern of the ceramic when $\sigma_0 = 0$ MPa and $\sigma_0 = -127$ MPa, respectively. Note that the fracture plane is the plane with the maximum tensile stress, suggesting failure here is governed by the maximum tensile stress. (For interpretation of the references to color in this figure legend, the reader is referred to the web version of this article.)

While the M–C failure criterion captures the fracture behavior in $Zr_{41}Ti_{14}Cu_{12.5}Ni_{10}Be_{22.5}$ metallic glass, we neglect that dilatancy effect during the plastic flow of the metallic glass. As pointed out by Anand and Su [26], shear induced dilatancy could be crucial in governing shear-band formation and propagation, which has long been recognized in the deformation of granular materials [41–43]. Indeed, free-volume generation or shear induced dilatation was regarded to influence the plastic flow of metallic glasses [28], in particular during confined deformation [26]. By considering the shear induced dilatancy, Anand and spitzig showed that the inclination angle of the shear band with respect the max principal stress direction θ is determined by the internal friction parameter α and the dilatancy parameter η, and predicts that [43]

$$\theta = \arctan\left[\sqrt[4]{\frac{(1+\alpha)(1+\eta)}{(1-\alpha)(1-\eta)}}\right] \tag{9}$$

Here η quantifies the difference between the averaged atomic cage volume in a metallic glass during deformation and the cage volume in a state of dense random packing, and is on the order of one hundredth. We apply $\alpha = 0.058$ and $\eta = 0$ and $\eta = 0.05$ to Eq. (9) to examine the dependence of the inclination angle θ on η, and we get $\theta = 45.83°$ and $\theta = 46.55°$ respectively. The values of η, as long as it is on the order of one hundredth, has negligible influence on the fracture angle. The small dependence of fracture angle on η is apparently seen in Eq. (9) as $[(1+\eta)/(1-\eta)]^{0.25}$ would be rather small if η is on the order of one hundredth.

We note that spiral fracture can be utilized to reveal the deformation mechanisms of other materials like ductile metals and brittle ceramics. In Fig. 6, we show the mechanical response of ductile Al 6061 and brittle ceramic Al_2O_3 under combined shear and normal stresses. The plastic deformation and failure in Al 6061 is consistent with typical failure mode in materials governed by Mises type of plastic flow. Detailed analysis about the deformation pattern induced by Mises type of plastic flow or the maximum shear stress flow (also known as Mohr criterion where the frictional part in the Mohr–Coulomb criterion is not considered) in tubes subjected to torsion–tension was given by Taylor and Quinney in 1931 [35]. In the ceramic Al_2O_3, we also see the evolution of spiral fracture at different normal stresses. It is straightforward to validate that the fracture plane is the plane with the maximum tensile stress, suggesting failure here is governed by the maximum tensile stress. This is consistent with much previous work on the effects of changes in stress state on flow and fracture, recently reviewed by Lowhaphandu et al. [7].

4. Conclusion

To conclude, we performed comprehensive experimental investigation on the failure of BMGs subjected to both shear and normal stress. Our work leads to the finding of spiral fracture in Vitreloy 1 subjected to both shear and normal stresses. The M–C criterion, using an internal friction coefficient of $\alpha = 0.058 \pm 0.012$ and a cohesion of $c = 1.026 \pm 0.014$ GPa, predicts the experimental strength envelope well at all range of normal stress. This value of $\alpha = 0.058 \pm 0.012$ is very consistent with other tests conducted with superimposed hydrostatic pressure [1,3–7]. In contrast, predictions by the other criteria deviate apparently from experiments, in particularly when the normal stress approaches the compressive strength of Vitreloy 1. We further validate self-consistently the M–C criterion, by examining its predictability to the spiral fracture angles as a function of the applied normal stress. Our contrast experiments suggest that the critical combination of normal–shear stresses leading to failure is independent on loading path. While dilatation might have played an important role for the formation of localized deformation, we see that it exhibits negligible influence on the fracture angle as long as it is on the order of one hundredth. Our results showed here lead to a novel experimental strategy to examine critically the applicability of different strength criteria to metallic glass and other materials.

Acknowledgments

The authors acknowledge support from National Natural Science Foundation of China (NSFC) (11425211, 11021262, 11272327), MOST 973 of China (2012CB937500). The authors are grateful to Prof. J. Lewandowski and Prof. A. Lindsay Greer for fruitful discussion.

References

[1] L.A. Davis, S. Kavesh, Deformation and fracture of an amorphous metallic alloy at high-pressure, J. Mater. Sci. 10 (1975) 453–459.
[2] M.M. Trexler, N.N. Thadhani, Mechanical properties of bulk metallic glasses, Prog. Mater. Sci. 55 (2010) 759–839.
[3] J. Caris, J.J. Lewandowski, Pressure effects on metallic glasses, Acta Mater. 58 (2010) 1026–1036.
[4] P. Lowhaphandu, S.L. Montgomery, J.J. Lewandowski, Effects of superimposed hydrostatic pressure on flow and fracture of a Zr–Ti–Ni–Cu–Be bulk amorphous alloy, Scr. Mater. 41 (1999) 19–24.
[5] P. Lowhaphandu, L.A. Ludrosky, S.L. Montgomery, J.J. Lewandowski, Deformation and fracture toughness of a bulk amorphous Zr–Ti–Ni–Cu–Be alloy, Intermetallics 8 (2000) 487–492.
[6] J.J. Lewandowski, P. Lowhaphandu, Effects of hydrostatic pressure on the flow and fracture of a bulk amorphous metal, Philos. Mag. A 82 (2002) 3427–3441.
[7] J.J. Lewandowski, P. Lowhaphandu, Effects of hydrostatic pressure on mechanical behaviour and deformation processing of materials, Int. Mater. Rev. 43 (1998) 145–187.
[8] C.A. Schuh, T.C. Hufnagel, U. Ramamurty, Overview no.144 – mechanical behavior of amorphous alloys, Acta Mater. 55 (2007) 4067–4109.
[9] P.W. Bridgman, Studies in Large Plastic Flow and Fracture with Special Emphasis on the Effects of Hydrostatic Pressure, McGraw-Hill, New York, 1952.
[10] P.E. Donovan, A yield criterion for $Pd_{40}Ni_{40}P_{20}$ metallic glass, Acta Metall. 37 (1989) 445–456.
[11] G. Sunny, J.J. Lewandowski, V. Prakash, Effects of annealing and specimen geometry on dynamic compression of a Zr-based bulk metallic glass, J. Mater. Res. 22 (2007) 389–401.
[12] G. Sunny, F. Yuan, V. Prakash, J.J. Lewandowski, Design of inserts for split-Hopkinson pressure bar testing of low strain-to-failure materials, Exp. Mech. 49 (2009) 479–490.
[13] J. Lu, G. Ravichandran, Pressure-dependent flow behavior of $Zr_{41.2}Ti_{13.8}Cu_{12.5}Ni_{10}Be_{22.5}$ bulk metallic glass, J. Mater. Res. 18 (2003) 2039–2049.
[14] H.A. Bruck, T. Christman, A.J. Rosakis, W.L. Johnson, Quasi-static constitutive behavior of $Zr_{41.25}Ti_{13.75}Ni_{10}Cu_{12.5}Be_{22.5}$ bulk amorphous alloys, Scr. Metall. Et Mater. 30 (1994) 429–434.
[15] K.M. Flores, R.H. Dauskardt, Fracture and deformation of bulk metallic glasses and their composites, Intermetallics 12 (2004) 1025–1029.
[16] K.M. Flores, R.H. Dauskardt, Mode II fracture behavior of a Zr-based bulk metallic glass, J. Mech. Phys. Solids 54 (2006) 2418–2435.
[17] R. Varadarajan, A.K. Thurston, J.J. Lewandowski, Increased toughness of zirconium-based bulk metallic glasses tested under mixed mode conditions, Metall. Mater. Trans. A 41A (2010) 149–158.
[18] A.C. Lund, C.A. Schuh, The Mohr–Coulomb criterion from unit shear processes in metallic glass, Intermetallics 12 (2004) 1159–1165.
[19] A.C. Lund, C.A. Schuh, Yield surface of a simulated metallic glass, Acta Mater. 51 (2003) 5399–5411.
[20] C.A. Schuh, A.C. Lund, Atomistic basis for the plastic yield criterion of metallic glass, Nat. Mater. 2 (2003) 449–452.
[21] R. Vaidyanathan, M. Dao, G. Ravichandran, S. Suresh, Study of mechanical deformation in bulk metallic glass through instrumented indentation, Acta Mater. 49 (2001) 3781–3789.
[22] M.N.M. Patnaik, R. Narasimhan, U. Ramamurty, Spherical indentation response of metallic glasses, Acta Mater. 52 (2004) 3335–3345.
[23] V. Keryvin, Indentation of bulk metallic glasses: relationships between shear bands observed around the prints and hardness, Acta Mater. 55 (2007) 2565–2578.
[24] J. Fornell, A. Concustell, S. Surinach, W.H. Li, N. Cuadrado, A. Gebert, M.D. Baro, J. Sort, Yielding and intrinsic plasticity of Ti–Zr–Ni–Cu–Be bulk metallic glass, Int. J. Plast. 25 (2009) 1540–1559.
[25] D.C. Drucker, W. Prager, Soil mechanics and plastic analysis for limit design, Q. Appl. Math. 10 (1952) 157–165.
[26] L. Anand, C. Su, A theory for amorphous viscoplastic materials undergoing finite deformations, with application to metallic glasses, J. Mech. Phys. Solids 53 (2005) 1362–1396.
[27] M. Zhao, M. Li, Interpreting the change in shear band inclination angle in metallic glasses, Appl. Phys. Lett. 93 (2008) 241906.
[28] F. Spaepen, Microscopic mechanism for steady-state inhomogeneous flow in metallic glasses, Acta Metall. 25 (1977) 407–415.
[29] P. Thamburaja, B. Klusemann, S. Adibi, S. Bargmann, The plastic yield and flow behavior in metallic glasses, Appl. Phys. Lett. 106 (2015) 051903.
[30] Z.F. Zhang, G. He, J. Eckert, L. Schultz, Fracture mechanisms in bulk metallic glassy materials, Phys. Rev. Lett. 91 (2003) 045505.
[31] Y. Chen, M.Q. Jiang, Y.J. Wei, L.H. Dai, Failure criterion for metallic glasses, Philos. Mag. 91 (2011) 4536–4554.
[32] Y. Wei, An extended strain energy density failure criterion by differentiating volumetric and distortional deformation, Int. J. Solids Struct. 49 (2012) 1117–1126.
[33] Y. Wei, The intrinsic and extrinsic factors for brittle-to-ductile transition in bulk metallic glasses, Theor. Appl. Fract. Mech. 71 (2014) 76–78.
[34] X.Q. Lei, C.L. Li, X.H. Shi, X.X. Xu, Y.J. Wei, Notch strengthening or weakening governed by transition of shear failure to normal mode fracture, Sci. Rep. 5 (2015) 10537.
[35] G.I. Taylor, H. Quinney, The plastic distortion of metals, Philos. Trans. Roy. Soc. Lond. A230 (1932) 323–362.
[36] R.J. Asaro, J.R. Rice, Strain localization in ductile single-crystals, J. Mech. Phys. Solids 25 (1977) 309–338.
[37] Y.J. Wei, X.Q. Lei, L.S. Huo, W.H. Wang, A.L. Greer, Towards more uniform deformation in metallic glasses: the role of Poisson's ratio, Mater. Sci. Eng. A 560 (2013) 510–517.
[38] W.F. Wu, Y. Li, C.A. Schuh, Strength, plasticity and brittleness of bulk metallic glasses under compression: statistical and geometric effects, Philos. Mag. 88 (2008) 71–89.
[39] J.H. Yao, J.Q. Wang, L. Lu, Y. Li, High tensile strength reliability in a bulk metallic glass, Appl. Phys. Lett. 92 (2008) 041905.
[40] M.Q. Jiang, Z. Ling, J.X. Meng, L.H. Dai, Energy dissipation in fracture of bulk metallic glasses via inherent competition between local softening and quasi-cleavage, Philos. Mag. 88 (2008) 407–426.
[41] J.W. Rudnicki, J.R. Rice, Conditions for the localization of deformation in pressure sensitive dilatant materials, J. Mech. Phys. Solids 23 (1975) 371–394.
[42] I. Vardoulakis, Shear band inclination and shear modulus of sand in biaxial tests, Int. J. Numer. Anal. Meth. Geomech. 4 (1980) 103–119.
[43] L. Anand, W.A. Spitzig, Shear-band orientations in plain strain, Acta Metall. 30 (1982) 553–561.